$0{\cdot}36\,\mu m$ has an effective index of $n_e = 1{\cdot}73$. If we further assume a nonresonant pump, $\omega = 5\,\mu m$, $l = 100\,\mu m$, $d_{eff} = d_{11} = 250\,pm/V$, and $T_1^{2\omega} = \hat{T}_1^{2\omega} = \delta^{2\omega} = 0{\cdot}01$, and use eqn. 11 we find $P_{out}/P_{inc}^2 = 0{\cdot}05\,W^{-1}$. Because $m = 3$, we expect the efficiency to be approximately nine times larger if quasi-phasematching is employed (numerically we obtain a factor of 13·4), which gives $P_{out}/P_{inc}^2 = 0{\cdot}66\,W^{-1}$.

If both the pump and the second harmonic are resonant, the assumption of low conversion efficiency is no longer valid for an incident power of the order of 100 mW, as is easily seen from the above numerical result. In such cases, eqn. 11 is no longer valid, and the exact solution to eqns. 9 and 10 must be used. We give a numerical example here, reserving a more detailed analysis for future work. Assuming $A_1^{\omega} = A_1^{2\omega} = 0{\cdot}005$, $\delta^{\omega} = 0{\cdot}05$, no quasi-phasematching, and $P_{inc} = 100\,mW$ in addition to the above parameters, we find a maximum second harmonic power output of 36 mW for an optimal coupling given by $T_1^{\omega} = \hat{T}_1^{\omega} = 0{\cdot}097$, and $T_1^{2\omega} = \hat{T}_1^{2\omega} = 0{\cdot}027$. We see that high conversion efficiencies are possible for modest input power, and that the optimal coupling differs from that calculated in the low efficiency regime.

Conclusion: We have shown that vertical cavity resonant SHG structures can have significantly higher conversion efficiency than conventional surface emitting SHG devices, and have identified $d_{eff}^2/n_{\omega}^2 n_{2\omega}\alpha_{\omega}^2\alpha_{2\omega}$ as the relevant material figure of merit for a doubly resonant interaction. A phase-matchable nonlinearity is not necessary, as seen in the numerical example where tens of milliwatts of second harmonic were obtained for a 100 mW pump using the nonphase-matchable d_{11} coefficient of MNA. The efficiency may be significantly increased over that calculated here if quasi-phasematching techniques can be applied in this resonant geometry. Extension of this theory to TM modes, multilayer waveguides and interactions such as parametric amplification and oscillation will be given elsewhere.

Acknowledgments: This work is supported in part by DARPA, under contract number MDA972-90-C-0046, and R. Lodenkamper gratefully acknowledges the support provided by AT&T.

R. LODENKAMPER
M. M. FEJER*
J. S. HARRIS, JUN.

Solid State Laboratory
Stanford University
Stanford, CA 94305, USA

29th July 1991

**Edward L. Ginzton Laboratory*
Stanford University
Stanford, CA 94305, USA

References

1 VAKHSHOORI, D., WU, M. C., and WANG, S.: 'Surface-emitting second-harmonic generator for waveguide study', *Appl. Phys. Lett.*, 1988, **52**, (6), pp. 422–424
2 NORMANDIN, R., WILLIAMS, R. L., and CHATENOUD, F.: 'Enhanced surface emitting waveguides for visible, monolithic semiconductor laser sources', *Electron. Lett.*, 1990, **26**, (25), pp. 2088–2089
3 ASHKIN, A., BOYD, G. D., and DZIEDZIC, J. M.: 'Resonant optical second harmonic generation and mixing', *IEEE J. Quantum Electron.*, 1966, **QE-2**, (6), pp. 109–123
4 LIAO, C., BUNDMAN, P., and STEGEMAN, G. I.: 'Second harmonic generation with surface guided waves in signal processing geometries', *J. Appl. Phys.*, 1983, **54**, (11), pp. 6213–6217
5 ZIMMERMANN, C., KALLENBACH, R., and HÄNSCH, T. W.: 'Doubly-resonant second-harmonic generation in β-barium borate', *Opt. Commun.*, 1989, **71**, (3, 4), pp. 229–234
6 LEVINE, B. F., BETHEA, C. G., DRUMMOND, C. D., LYNCH, R. T., and BERNSTEIN, J. L.: 'An organic crystal with an exceptionally large optical second-harmonic coefficient: 2-methyl-4-nitroaniline', *J. Appl. Phys.*, 1979, **50**, (4), pp. 2523–2527
7 SASAKI, K., KINOSHITA, T., and KARASAWA, N.: 'Second harmonic generation of 2-methyl-4-nitroaniline by a neodymium : yittrium aluminum garnet laser with a tapered slab-type optical waveguide', *Appl. Phys. Lett.*, 1984, **45**, (4), pp. 333–334
8 YEH, P.: 'Optical waves in layered media' (Wiley, New York, 1988)
9 SNYDER, A. W., and LOVE, J. D.: 'Optical waveguide theory' (Chapman and Hall, London, 1983)

REVERSE HUFFMAN TREE FOR NONUNIFORM TRAFFIC PATTERN

Indexing terms: Codes and coding, Digital communication systems, Communication networks

The tree protocol has been an important protocol in multiaccess communication channels with traffic that arrives uniformly. In the Letter, a reverse Huffman tree protocol is proposed for multiaccess networks with nonuniform traffic pattern. Some tree construction protocols are developed and reverse Huffman tree protocol is shown to have the smallest delay.

Introduction: This Letter considers the multiple accessing of a broadcast channel by a set of independent stations. For broadcast channels, the resolution of channel contention is the heart of the multiaccessing problem, and the tree protocol provides a good solution.[1–4] However, the original tree protocol was designed for systems with uniform arrival rates.

In this Letter, a system with nonuniform arrival rates is considered. Because each station has its own traffic intensity which may be different from others, different structures may influence the average packet delay. The packet delay is a major issue of the system performance and is defined as the time from the instant that a packet arrives at a source to the instant that it is successfully received by its destination.

To build the tree for a system with nonuniform traffic pattern, we apply the coding schemes developed from coding theory to construct the tree. We notice that Huffman coding, the best coding scheme which minimises the average code length, has a good performance but does not achieve the best performance. Hence, we propose another scheme called the reverse Huffman code tree which achieves a better performance than the Huffman code tree.

Tree types and simulation results: We first propose four schemes in constructing the tree structure. We then run simulations to show and compare the performances of different schemes. To provide an example, we let $\vec{\lambda} = (1, 5, 6, 9, 12, 18, 23, 40)$. Note that the overall system arrival rate cannot exceed unity to achieve a stable system, hence this $\vec{\lambda}$ is just a scaled vector which shows the relative ratio of packet arrival rates to all stations.

(i) *Random:* In this method, we construct a balanced tree and randomly map stations to tree leaves.

(ii) *Low traffic first tree:* In this method, we build a balanced tree and map stations to tree leaves in an ascending order of the traffic arrival rates. Clearly, the delay performance of this tree will be poor and we will use it as the worst case in the performance comparison.

(iii) *Huffman code tree:* With one Huffman code method,[5] we can obtain a good tree structure and mapping. We arrange λ_i in a descending order and the depth d_i in an ascending order; i.e. we have both

$$\lambda_1 \leq \lambda_2 \leq \lambda_3 \leq \ldots \leq \lambda_N$$

and

$$d_1 \geq d_2 \geq d_3 \geq \ldots \geq d_N$$

Note that under this tree construction method, we minimise D over all structures where D is defined as $D = \sum_{i=1}^{N} \lambda_i d_i$. This D corresponds to the average code length in coding theory.

Algorithm:

(1) combine the two nodes with least transmission rates (j and k) into a dummy node; $\lambda_{dummy} = \lambda_j + \lambda_k$

(2) construct a binary tree; this dummy node is the father node, and the two corresponding nodes are descendants (left child and right child)

(3) delete λ_j and λ_k from $\vec{\lambda}$ and add λ_{dummy} to $\vec{\lambda}$; go to step 1

Fig. 1 is the tree structure and mapping from this algorithm.

(iv) *Reverse Huffman code tree:* In this scheme we try to divide a tree into two equal traffic subtrees at each intermediate node. We design a protocol which partitions a tree into two subtrees where the weights of the subtrees are as equal as possible. Because this protocol functions exactly in the opposite way to the Huffman code protocol, we call the tree derived from this protocol the reverse Huffman code tree.

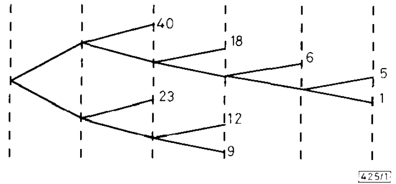

Fig. 1 *Tree derived from Huffman code algorithm*

Algorithm: RHT (reverse Huffman code tree construction):

(1) if the arrival rates of all stations have been divided into two sets (left set and right set); go to step 3

Else

Partition the two stations with greater arrival rates (j and k) into two different sets, and create a dummy node; $\lambda_{dummy} = \lambda_j - \lambda_k, \lambda_j \geq \lambda_k$

(2) delete λ_j and λ_k from $\vec{\lambda}$ and add λ_{dummy} to $\vec{\lambda}$; go to step 1

(3) construct a binary tree; left child and the right child correspond to two respective sets

(4) $\vec{\lambda}$ = left set; call RHT
$\vec{\lambda}$ = right set; call RHT

Fig. 2 is the tree structure of the reverse Huffman code tree construction protocol.

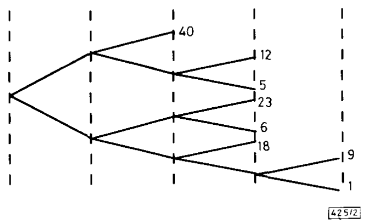

Fig. 2 *Tree derived from RHT*

Simulation results and comparisons of four tree types: We obtain the average delay of packets under the different tree types through simulations. Fig. 3 shows the average delay for the four different trees under the slotted ALOHA environment. In this Figure, we show that the performance of the different tree types can differ significantly.

In Fig. 3, many interesting points are observed. First, the performance order of these four tree types is (4) > (3) > (1) > (2). It shows that the reverse Huffman code protocol is the best. Secondly, we intuitively think that the Huffman code algorithm should have the best performance because it has the smallest D. In fact, this $D = \sum_{i=1}^{N} \lambda_i d_i$ is the average tree length but the delay is partly determined by this parameter. That is, the minimum D of the original tree does not imply the minimum delay of the actual contention tree. Nonetheless, a tree with small D has a small packet delay as the performance of the Huffman tree shows. Thirdly, the reverse Huffman tree has the characteristic of balanced arrival rates of each subtree at each node; hence, the more balanced the arrival rates of the subtrees at each node, the lower is the delay of the packets.

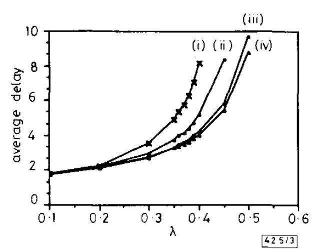

Fig. 3 *Average delay against overall λ for four protocols in slotted ALOHA*

(i) low traffic first
(ii) random
(iii) Huffman code
(iv) reverse Huffman code

Impact of traffic pattern on mean system time: We consider how the distribution of traffic pattern influences the system behaviour. Two systems with extreme traffic patterns are proposed of all traffic patterns. One extreme traffic pattern considered has all traffic concentrated in one station but no traffic in the others, i.e. $\vec{\lambda} = (1, 0, 0, \ldots, 0)$. For such a system, no contention may occur and its performance is exactly like an M/D/1 queueing system. The other extreme case is the uniform traffic system in which all stations have the same arrival rate; i.e. $\vec{\lambda} = (1, 1, 1, \ldots, 1)$.

We define $\bar{\lambda}$ as the average arrival rate at all stations and C_λ as the coefficient of variation of the traffic. Let the square of C_λ be represented as follows:

$$C_\lambda^2 = \frac{\sum_{i=1}^{N} (\lambda_i - \bar{\lambda})^2 \cdot \frac{1}{N}}{\bar{\lambda}^2}$$

In an M/D/1 system, $C_\lambda^2 = N - 1$ (N is the number of stations); for the uniform traffic system, $C_\lambda^2 = 0$. Because these are the extreme cases, C_λ^2 for all other traffic patterns ranges between 0 and $N - 1$. Certainly, the value of C_λ^2 indicates the variation of traffic pattern among all stations. The traffic pattern is more uniform with smaller C_λ^2. In the simulation results shown in Fig. 4, we will only examine systems at heavy loads because the system delay rises sharply at heavy load and that is the case to which we should pay more attention. In the simulations, we use the reverse Huffman code tree algorithm and the low traffic first tree algorithm to show the average delay against C_λ^2 because they are the best and the worst tree structures of the four different tree types described above.

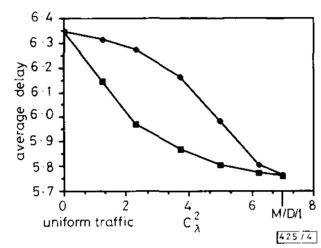

Fig. 4 *Average delay against C_λ^2*

—■— reverse Huffman code
—◆— low traffic first
$\lambda = 0.9, \beta = 0.01, N = 8$

There are two observations concerning Fig. 4. First, when the system is at heavy load, the larger C_λ^2 is, and the smaller the average delay becomes. In other words, the system with more uniform traffic pattern has a higher average delay if all other conditions are the same. Secondly, the more balanced the weight of the tree, the less the delay of the system. It is these observations which confirm our conclusion that a good tree structure is important in achieving a good system performance if the traffic pattern is nonuniform.

Conclusion: In this Letter, we applied the tree algorithm to a network with finite number of stations with nonuniform traffic. We examined the delay characteristics of different tree structures and studied how the types of tree influence the system delay. From these results, we learn that it is important to choose the correct tree structure to avoid too many collisions. Hence, a reverse Huffman tree is proposed which has the best delay performance.

J.-H. HUANG
Y.-C. LAI

Department of Computer Science and Information Engineering
National Taiwan University
Taipei, Taiwan, Republic of China

26th July 1991

References

1 CAPETENAKIS, J. I.: 'Tree algorithms for packet broadcast channels', *IEEE Trans.*, 1979, **IT-25**, pp. 505–515
2 MATHYS, P., and FLAJOLET, P.: 'Q-ary collision resolution algorithms in random-access systems with free or blocked channel access', *IEEE Trans.*, Mar. 1985, **IT-31**
3 MERAKOS, L. F., and BISDIKIAN, C.: 'Delay analysis of the n-ary stack random-access algorithm', *IEEE Trans.*, September 1988, **IT-34**, pp. 931–942
4 KAPLAN, M. A., and GULKO, E.: 'Analytic properties of multiple-access trees', *IEEE Trans.*, March 1985, **IT-31**, pp. 255–263
5 LYNCH, T. J.: 'Data compression: techniques and applications' (Wadsworth, Inc., 1985)

15 GHz f_{max} MICROWAVE SILICON *pnp* TRANSISTORS WITH SINGLE-CRYSTAL EMITTERS FABRICATED WITH SIMPLE FOUR MASK PROCESS

Indexing terms: Transistors, Microwave devices and components, Semiconductor devices and materials

Vertical *pnp* transistors have been fabricated using a four mask, low cost quasi-selfaligned process with submicrometre feature sizes. The resulting monocrystalline emitter devices achieve f_t greater than 9 GHz and f_{max} greater than 15 GHz with BV_{ceo} greater than 13 V. These discrete *pnps* were used successfully as active loads for a monolithic *npn* opamp to achieve a gain-bandwidth product of 4·4 GHz.

Introduction: As the performance of discrete and integrated *npn* transistors is improved through technology and device innovations, a need arises for improved complementary devices (*pnp* devices) so that analogue circuits with features such as active loads, level shifters etc. (see, for example, Reference 1) may be realised at gigahertz frequencies.

pnp transistors have a few physical and technological intrinsic drawbacks when compared to *npn* transistors. The saturated drift velocity (collector) and the mobility (base) of holes are lower than that of electrons, and shallow emitters are difficult to realise due to the high boron diffusivity. Even so, impressive f_t values have recently been reported[2,3] using selfaligned double polysilicon processes or thin epitaxial SiGe base technologies. Because polysilicon emitters are not ideal for high-precision analogue applications, due to high emitter resistance for example, and because epitaxial base technologies have not yet matured, a high yield fabrication process which realises monocrystalline emitter high-frequency *pnp* transistors has been developed.

Process description: The four mask SAT (selfaligned discrete transistor) process flow is shown in Fig. 1. After growth of a boron doped epitaxial collector layer (two collector types used: an 'analogue' version with 1·4 μm thickness and 6×10^{15} cm^{-3} doping, and a 'mixed analogue/digital' version with 0·9 μm thickness and $1{\cdot}5 \times 10^{16}$ cm^{-3} doping) on a P^+ $\langle 111 \rangle$ Si substrate, a thin thermal oxide/LPCVD silicon nitride stack is formed on the wafer surface. A standard recessed local oxidation of Si (LOCOS) process is then carried out to define the device regions. This consists of dry etching of the silicon nitride/thin-oxide stack and approximately 1 μm of the Si from the field region, after which a 2 μm field oxide is grown by wet oxidation at 1000°C. Following this, the base layer is formed by ion implantation of arsenic (As^+, 180 keV, 4×10^{15} cm^{-2}) through the silicon nitride/thin-oxide stack which remains on the device islands following LOCOS. After an anneal step selected to form a collector–base junction depth of approximately 0·3 μm, a photomask step with non-critical alignment is used to define both the emitter and base contacts (Fig. 1*a*). This simultaneous definition of both electrodes allows the use of the minimum dimension (0·7 μm using contact lithography), with a minimal emitter-to-base spacing as no alignment is necessary. The exposed nitride/thin-oxide regions are then dry etched (Fig. 1*b*). This is followed by boron ion implantation (BF_2^+, 35 keV, 5×10^{15} cm^{-2}) to form the emitters (Fig. 1*b*). Because emitter dopant was also implanted in the base contacts, an emitter shield mask is now defined (Fig. 1*c*) such that a light Si etch may be carried out to subtract BF_2^+ from the base contacts. Again, the alignment is noncritical. Arsenic is then ion implanted (As^+, 40 keV, 4×10^{15} cm^{-2}) into the base contact openings to create N^{++} contacts (Fig. 1*d*). Following a wafer clean, the emitter is driven in using rapid thermal annealing (RTA) in an argon ambient. A TiW/Au metallisation is carried out to form the interconnect (Fig. 1*e*), before passivating the devices with plasma silicon nitride. The above process flow is similar to

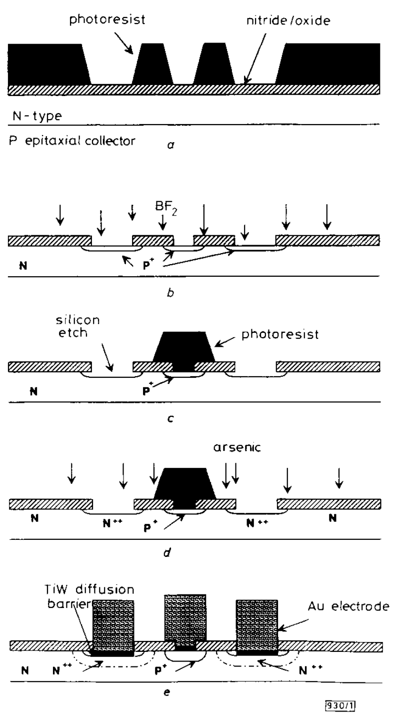

Fig. 1 *Flow of four mask quasi-selfaligned SAT silicon bipolar transistor process*

Shown are device cross-sections at critical processing steps
a Photomask step
b Dry etching, boron implantation
c Emitter shield mask definition
d Arsenic ion implantation to create N^{++} contacts
e TiW/Au metallisation